Seismic Test of Solar Models, Solar Neutrinos and Implications for Metal-Rich Accretion

R. A. Winnick, Pierre Demarque and Sarbani Basu

Department of Astronomy, Yale University, Box 208101, New Haven, CT 06520-8101

and

D. B. Guenther

Department of Astronomy and Physics, Saint Mary's University, Halifax, NS, Canada, B3H 3C3

ABSTRACT

The Sun is believed to have been the recipient of a substantial amount of metal-rich material over the course of its evolution, particularly in the early stages of the Solar System. With a long diffusion timescale, the majority of this accreted matter should still exist in the solar convection zone, enhancing its observed surface abundance, and implying a lower-abundance core. While helioseismology rules out solar models with near-zero metallicity cores, some solar models with enhanced metallicity in the convection zone might be viable, as small perturbations to the standard model. Because of the reduced interior opacity and core temperature, the neutrino flux predicted for such models is lower than that predicted by the standard solar model. This paper examines how compatible inhomogeneous solar models of this kind are with the observed low and intermediate degree p-mode oscillation data, and with the solar neutrino data from the SNO Collaboration. We set an upper limit on how much metal-rich accretion took place during the early evolution of the Sun at $\sim 2 M_\oplus$ of iron (or $\sim 40 M_\oplus$ of meteoric material).

Subject headings: Sun: accretion, evolution, interior, oscillations, neutrinos

1. Introduction

Early on in the evolution of the Sun, the interstellar medium and young Solar System provided an environment capable of frequent accretion events. Material in the form of ISM,

proto-planets, planetesimals, comets, and asteroids frequently bombarded the Solar surface and were accreted. This accreted matter is deficient in hydrogen and helium, introducing metal-rich material into the upper layers of the Sun. Exactly how much metal-rich matter was accreted in these early stages and for how long, has been speculated by several authors (Christensen-Dalsgaard, Gough, & Morgan 1979, Jeffery et al. 1997), but unfortunately is not well known.

More recently, Murray et al. (2001) have searched a sample of 640 solar-type stars for the signature of iron enhancement in their spectra and concluded that, on average, these stars appear to have accreted about $0.5M_\oplus$ of iron while on the main sequence. They raise the possibility that the Sun may have accreted a similar amount of iron during its evolution. Whether helioseismology can detect this amount of accretion is uncertain. So far only one study has been published on the effect of accretion on the p-mode frequency (Henney & Ulrich 1998). These authors concluded that the accretion of $8M_\oplus$ of meteoric material (approximately $0.4M_\oplus$ of iron) on the Sun could not be detected by seismology due to other uncertainties in the models.

The main consequence of such accretion is the metal enrichment of the Sun's surface and convection zone, while maintaining a lower-abundance core. In such a scenario, the expected neutrino flux is reduced due to the lower opacity and temperature in the central region of the Sun. It has long been known that solar models with near-zero metallicity cores can lower the predicted neutrino flux, and this explanation was discussed early-on as a possible solution of the classical neutrino problem (see e.g. the review by Rood 1978). More recently, Guenther & Demarque (1997, hereafter GD97) have constructed solar models with low-Z cores using present physics and found their p-mode frequencies to be incompatible with solar p-mode observations.

This paper describes work which can be viewed as an extension of GD97; but this time we examine the limits set by helioseismology on the non-standard assumption that the solar convection zone of the Sun has been enriched in heavy elements by accretion during its early evolution. In addition to comparing the p-mode frequencies to observation in the frequency difference diagram, as done by GD97, we also compare the calculated sound-speed and density in our models to the same quantities derived from observation by inversion (Basu & Antia 1997, hereafter BA97; Basu, Pinsonneault & Bahcall 2000, hereafter BPB00).

Since this research was begun, the first results from the Sudbury Neutrino Observatory (SNO) experiment have been released (Ahmad et al. 2001). Ahmad et al. (2001) conclude that the ^{8}B neutrino flux derived from their observations, i.e. $\Phi_{^8B} = 5.44 \pm 0.99 \times 10^6$ cm^{-2}s^{-1}, agrees with the predictions of the best standard solar models. Any accretion model must then also be constrained by the SNO observations, in addition to the constraints of

helioseismology.

2. Assumptions and Method

The main assumption in this paper is that the accretion of heavy elements onto the Sun took place during the early evolution of the Sun, at a time when the Sun was near the main sequence, i.e. when the convection zone had reached its main sequence value. The convection is shallow at this time, and only the outer 2% of the Sun's mass in the convection zone get enriched.

As in GD97, the solar models were constructed using the Yale stellar evolution code (YREC for Yale Rotating Evolution Code) in its non-rotating configuration (Guenther et al. 1992). The energy generation routines used in YREC are those of Bahcall & Pinsonneault (1992). The neutrino cross sections used are the same as in Bahcall, Pinsonneault & Basu (2001). The equation of state tables prepared by the OPAL researchers (Rogers 1986, Rogers, Swenson, & Iglesias 1996) were used for the models. The interior opacities were derived from the OPAL opacity tables (Iglesias & Rogers 1996), while the surface and atmospheric opacities were taken from the Alexander & Ferguson (1994) tables.

All models were evolved from a zero-age main sequence (ZAMS) model to near the age of the Sun in 50 equally spaced time steps. The age of the Sun was taken to be 4.5 Gyr, close to the meteoric solar age (Guenther 1989). As was noted by GD97, standard solar models of this age are in best agreement with the calculated oscillation spectra. The mixing length/pressure scale height ratio, α, and the helium content by mass, Y, were adjusted automatically by the code to produce a precisely calibrated standard solar model (Guenther et al. 1992). Most models were tuned to match the observed solar radius to one part in 10^7 ($R_\odot$=6.958 x 10^{10}cm) and the solar luminosity to one part in 10^6 ($L_\odot$=3.8515 x 10^{33}ergs s^{-1}). Models #15, 16, and 19 (see Table 1) did not converge at the aforementioned tolerance for radius, but converged to the solar radius to one part in 10^6. The number of shells in standard solar models #17 and 18 was 1892, and 1893 in models #19 and 20. There were more than 2300 shells in all non-standard solar models. Tests have shown that at least that many shells are needed to obtain the required precision in the calculation of the p-mode frequencies (Guenther et al. 1992; Guenther 1994).

Helium and heavy element diffusion were included in all of the solar models due to their necessary role in finding simultaneous agreement with both the observed value of $(Z/X)_\odot$ and the p-mode spectrum (for further details see GD97). The assumption made regarding the nonstandard models is that due to the accretion of metal-rich matter, the Sun's interior,

(defined here as $R < R_{env}$), is composed of material at a lower heavy-element abundance than the Sun's surface. In order to produce such nonstandard solar models with low-Z interiors, the run of Z in the initial ZAMS model was modified. The interior metal abundance was initially set to the homogeneous value of Z_{int} out to $(M/M_\odot)=0.9$, indicating a metal-poor interior. The more metal-rich exterior of the Sun, $(M/M_\odot)\geq0.975$, was setup with a metal abundance of Z_{init}. Z_{int} and Z_{init} represent ZAMS mass fractions of all heavy elements for the interior and exterior, respectively. In the intermediate region, $0.9\leq(M/M_\odot)\leq0.975$, Z linearly increases from Z_{int} to Z_{init}.

In deciding what value Z_{int} might be for the nonstandard solar models, it is relevant to note that the Sun is observed to be more metal rich than the surrounding ISM, with Z_{ISM} possibly as low as 65% of $Z_\odot$ (Mathis 1996). Believing the Sun formed from material typical of the ISM, the metal-enhanced exterior could have resulted from the bombardment of metal-rich material in the form of comets, asteroids, planetesimals and proto-planets. With a long diffusion timescale, most of this material should still exist in the upper layers of the Sun, leaving the interior metal-poor, much like the surrounding ISM. With this in mind, we chose a value of $Z_{int}=0.65Z_\odot$. Other values of $0.30Z_\odot$, $0.50Z_\odot$, and $0.80Z_\odot$ were also examined.

A choice of $Z_{int} = 0.80Z_{init}$ corresponds to an accretion enhancement of about $2M_\oplus$ in iron, or about $40M_\oplus$ in meteoric material. Similarly, $Z_{int}=0.65Z_{init}$, $Z_{int}=0.50Z_{init}$, and $Z_{int}=0.30Z_{init}$ corresponds to about $2.9M_\oplus$, $4.1M_\oplus$ and $5.7M_\oplus$, respectively, in iron accretion, or about $60M_\oplus$, $80M_\oplus$ and $120M_\oplus$, respectively, in meteoric material accretion.

Four standard solar models were created, differing only by the value of Z_{init}, the initial or ZAMS mass fraction value of all heavy elements in the solar exterior. Without the assumption of a more metal-poor interior, Z_{int} is assumed equivalent to Z_{init}. Values of Z_{init} were taken as 0.0170, 0.0188, 0.0200, and 0.0220. These standard solar models comprise models #17-20 in Tables 1-3. Z_{init} was also varied in the nonstandard solar models, thus along with the varying Z_{int}, a grid was created, comprising models #1-16 in Tables 1-3.

Physical characteristics of both the standard (#17-20) and nonstandard (#1-16) solar models are listed in Table 1. Table 1 includes, from left to right: Model, the model number; Type, the type of model, where NSSM stands for a nonstandard solar model and SSM stands for a standard solar model; X_{init}, the initial or ZAMS mass fraction value of hydrogen; Z_{init}, the initial or ZAMS mass fraction value of all heavy elements in the solar exterior; Z_{int}/Z_{init}, the initial or ZAMS mass fraction value of all heavy elements in the solar interior relative to Z_{init}; X_{surf}, the surface mass fraction value of hydrogen at the evolved age; Z_{surf}, the surface mass fraction of all heavy elements at the evolved age; M_{env}, the fraction of the total mass contained in the outer convective envelope; R_{env}, the radius fraction of the base of

the convective envelope; $\log P_c$, the base ten logarithm of the central pressure; $\log T_c$, the base ten logarithm of the central temperature; $\log \rho_c$, the base ten logarithm of the central density; X_c, the central mass fraction of heavy elements; Z_c, the central mass fraction of heavy elements.

The nuclear energy generation properties of both the standard (#17-20) and nonstandard (#1-16) solar models are listed in Table 2. Table 2 lists the fraction of total photon luminosity coming from the PP I, PP II, and PP III branches of the PP network and from the CNO cycle. Also listed are the individual neutrino fluxes from the neutrino producing reactions that occur in the sun (see Figure 1 of GD97). Note that in GD97 the neutrino fluxes are listed in units of $10^{10} \text{cm}^{-2}\text{s}^{-1}$. Finally, Table 2 lists $\Phi(^{37}\text{Cl})$, the total neutrino flux, in SNU, for the ^{37}Cl detector; and $\Phi(^{71}\text{Ga})$, the total neutrino flux, in SNU, for the ^{71}Ga detector.

3. p-mode Frequencies

As a test on the validity of a model, the expected oscillation frequencies can be compared with observations from the Sun. Guenther's non-radial, non-adiabatic pulsation program (Guenther 1994) was used to calculate the oscillation frequencies of the models produced with YREC. The model output was then compared with data obtained by the Michelson Doppler Imager (MDI) instrument on board the *Solar and Heliospheric Observatory (SOHO)* during the first year of its operation (Rhodes et al. 1997). This data set was chosen as it comprises one of the longest time-series of data, 360 days. More recent MDI-SOHO data include only 144-day or 72-day data sets, and therefore restrict the number of data points, with most sets having very few l=0,1,2 modes. Data from the GOLF experiment (see Bertello et al. 2000 and García et al. 2001 for the latest results) were not considered here despite the low-degree low-frequency modes. While these modes can tell us a lot about the structure of the core (see Turck-Chièze et al. 2001), for our purposes here, it requires mixing one set of low degree modes with intermediate and high degree modes from another instrument, which can give rise to artifacts in the solar core unless the data are contemporaneous (see Basu et al. 1996, 1997). Hence, in an attempt to avoid such artifacts, we have opted for a homogeneous set of data. For comparison, BiSON+LOWL (Basu et al. 1997) data were also used. This data set had been specially constructed by obtaining frequencies from contemporaneous BiSON and LOWL time series. This set gave results very similar to those obtained by the MDI-SOHO data set used here.

From these data, p-mode frequency differences: ν_{model}-$\nu_{\odot}$, were computed for l=0-4, 10, 20, 30, 40, 50, 60, 70, 80, 90, and 100. Frequency difference plots (model frequency minus

observed frequency versus observed frequency) were then constructed for each model and can be seen in Figure 1. Each line joins together data of a common l-value, hence joining together p-modes with approximately similar inner turning points. In the event of perfect seismic agreement with the Sun, a frequency difference plot would show a straight horizontal line at 0 μHz, indicating that the p-mode frequency differences were zero. Instead, Figure 1 shows a more complex bundle of lines, indicating discrepancies of our models from the Sun. As in GD97, the quality of a models' agreement with the Sun is judged on the tightness of the bundle of lines. The underlying slope error present is thought to be due to modeling errors in the very outermost layers of the Sun, a region of known uncertainties. The errors in the interior of the model, primarily near the base of the convection zone, are directly correlated to the bundle thickness in the sense that the tighter the bundle, the better the model is at fitting the region near and above the convection zone. (See GD97 for further details.)

Figure 1 is a 4×5 grid of plots showing the frequency differences for each of the 20 models computed. Each plot is annotated by its model number (see Tables 1-3), the surface Z/X ratio, and ^{8}B neutrino flux, in $cm^{-2}s^{-1}$. Lines connect common l-values, with l=0-4, 10, 20, 30, 40, 50, 60, 70, 80, 90, and 100. As indicated by the model numbers, the four standard solar models computed in this work comprise the last row in Figure 1. Figure 2 shows a larger version of the frequency-difference plot for model #20, including error bars from the MDI-SOHO data. The error bars indicate 10σ errors in the data averaged over 250μHz frequency bins, for all l-values included in this work. As can be seen in Figure 2, the errors increase with increasing frequency. Despite the relatively good agreement of our model with the Sun, the accuracy of the observations is such that our best model is discrepant at roughly the 30σ level at low frequencies, and is worse at higher frequencies. This large discrepancy seen in the calculated frequencies is not found in the sound speed comparison (see Figure 6). It is primarily due to modeling errors in the surface layers of the Sun, which could be reduced by further analyses including magnetic fields, turbulence, and a better understanding of the convection zone.

Special consideration was given to low l p-modes due to their ability to probe the deep interior of the Sun. This is due to the fact that the inner turning points of these modes are located closest to the core. Low l p-modes are still sensitive to the outer layers, but this effect can be canceled out by subtracting from a given p-mode frequency the frequency of a p-mode with a similar eigenfunction shape in the outer layers and distinct eigenfunction shape in the deeper layers. The small spacing difference, defined as $\delta\nu(n,l) = \nu(n,l) - \nu(n-1,l+2)$, thus provides a further diagnostic of the deep interior of the Sun. (See GD97 for further details.) To compare our models with observations from the Sun, small spacing differences plots were produced [i.e., $\delta\nu_{\mathrm{model}}(n,l) - \delta\nu_{\odot}(n,l)$ $vs.$ $\nu_{\odot}(n,l)$]. As in the case of the frequency difference

plots, the closer $\delta\nu_{\mathrm{model}}(n,l) - \delta\nu_{\odot}(n,l)$ is to 0 μHz, the better the agreement between the observations and a model.

Since the sensitivity of the small spacings to the deep interior of the Sun diminishes with increasing l, only those p-modes with l=0, 1, and 2 were used to contrast the models with observed values from the Sun. The small spacing difference plots can be seen in Figure 3. Figure 3 is a 3×5 grid in which each row contains models of the same Z_{int}, where Z_{int}=0.30Z_{init} includes models #1-4, Z_{int}=0.50Z_{init} includes models #5-8, Z_{int}=0.65Z_{init} includes models #9-12, Z_{int}=0.80Z_{init} includes models #13-16, and Z_{int}=Z_{init} includes the standard solar models #17-20. Each column in Figure 3 contains results for a common l-value, with l=0 in column 1, l=1 in column 2, and l=2 in column 3. Lines in each panel represent models with the same Z_{int} with differing Z_{init} values ranging from 0.0170 to 0.0220, as indicated.

4. Sound-speed and Density

Figure 4 shows the relative sound-speed differences for the twenty models presented in this paper compared to the observed solar sound-speed, derived from an inversion of the solar p-mode frequencies (BPB00). We note the superior agreement of the standard solar models with observation, especially model #20, as compared to the non-standard models. Similarly, Figure 5 shows the same plots for density. The less precise agreement with densities than with sound-speed is in part a reflection of the greater uncertainty in density inversions.

5. Solar Models

5.1. Choice of a Benchmark Standard Solar Model

Figure 1 shows the characteristics of the standard solar models (#17-20) in the frequency difference diagram. Best agreement with observation, as measured by the thickness of the line bundles corresponding to different l-values, favors #20 and 19. Note that our model #19 is nearly identical to model #20 of GD97, that was judged by GD97 as the "best" standard solar model in their study. But our model #20, which is intermediate in Z_{init} between GD97's models #20 and 21, is a better model still. The bundle of l-values in model #20 is thinner than in model #19, a fact which is also reflected in the best agreement with observation in the sound-speed plot shown in Figure 4.

In selecting a "best" standard solar model, one should also take into account two additional constraints. The first constraint, to which we will assign the most weight, is the solar

convection zone depth, R_{env}, which has been derived by sound-speed inversion (Christensen-Dalsgaard et al. 1991; BA97). The second additional constraint is Y_{surf} for the Sun. This quantity has also been estimated by inversion of the p-mode data (Basu 1998).

For model #20, we have $R_{env} = 0.7128$, to be compared to $R_{env} = 0.713 \pm 0.001$ from inversion (BA97). This agreement is confirmed by the sound-speed plot for model #20 (see Figures 4 and 7), which shows close agreement with the inversion data. At the same time, model #20 yields $Y_{surf} = 0.2519$, to be compared to the helium mass fraction 0.248 ± 0.003 derived by Basu (1998), a satisfactory agreement in view of the uncertainties in diffusion coefficients and efficiency. In addition, the ^{8}B neutrino flux of 5.63 cm^{-2}s^{-1} for model #20 is in excellent agreement with $\Phi_{^8B} = 5.44 \pm 0.99 \times 10^6$ cm^{-2}s^{-1} found by SNO (Ahmad et al. 2001). On the other hand, the surface metallicity $(Z/X)_{surf}$ is a little too large. One can see that a model interpolated between models #20 and 19 would satisfy all constraints within the errors.

As it is, model #20 is an excellent standard solar model, as illustrated in Figures 4-8. Comparing Figures 2 and 3 in BPB00 with our Figures 7 and 8, we see that model #20 compares favorably with model BP2000.

The small spacing plots (Figure 3) shows that all our standard models, models #17-20, agree equally well with observation. Within the range of chemical composition we have considered, small spacings are insensitive to the choice of initial heavy element content. Figure 6 shows the zoomed-in small spacing plot for $l=0$ for standard solar model #20. Error bars calculated from the MDI-SOHO data set used are also plotted. The observational uncertainties are approximately ± 0.07 μHz for the small spacing determination. From this figure, the numerical uncertainties in the solar model appear to be approximately ± 0.05 to 0.10 μHz for the small spacing calculation. The larger uncertainties of ± 1 μHz for the mode frequencies themselves cancel out somewhat when calculating the small spacings.

It is difficult to evaluate the uncertainty in the observed solar heavy element content $(Z/X)_{surf}$. GD97 used $(Z/X)_{surf} = 0.0244 \pm 0.001$, from Grevesse, Noels & Sauval (1996). More recent lower estimates suggest that large systematic errors may still exist in the measurements. Grevesse & Sauval (1998) find $(Z/X)_{surf} = 0.0230$, quoting a 10% error estimate. Asplund (2000), using a stellar model atmosphere constructed with a more realistic treatment of convection, derives $(Z/X)_{surf} = 0.0226$. Unfortunately, theoretical estimates for both Y_{surf} and $(Z/X)_{surf}$ are also difficult to make, due to the uncertainties in calculating the efficiency of diffusion just below the convection zone in the stellar interior (Chaboyer et al. 1995). Helioseismic sound-speed inversion shows that the tachocline structure is one of the least well-understood features of standard solar models (BA97).

5.2. Non-Standard Solar Models

At first glance, the frequency difference diagram in Figure 1 does not reveal much difference in bundle thickness between the non-standard models #7, 8, 11, and 15 and the standard model #19. The l-value bundle for model #12 seems even slightly thinner. But models #7, 8, 11 and 12 are all readily ruled out by the ^{8}B neutrino constraint.

Non-standard model #16 is similar to standard model #20 in having the thinnest l-value bundles and a marginal value for $(Z/X)_{surf}$. But it fails the ^{8}B neutrino test by a small amount. Non-standard models #10 and 15, like standard model #20, pass the convection zone depth test, but of these, only #15 passes the $(Z/X)_{surf}$ test. However, model #15 fails the ^{8}B neutrino test.

Turning to the small spacing diagram (Figure 3), we see that the non-standard models agree as well with observation as the standard models only for $l = 0$. But for $l = 1$ and $l = 2$, there is an increasing discrepancy with decreasing Z_{int}. The maximum discrepancy is only 2 μHz, however, which may still be within the uncertainties. As in the case of the standard models, heavy element content plays little role.

As a further comparison of the models calculated here, the root-mean-square of the sound-speed difference, rms$(\delta c/c)$, was computed for each model. Seen in Table 3, the results indicate that those models with Z_{init}=0.0220 fair well. Model #20 certainly outperforms the others, followed by standard solar model #19 and non-standard solar model #16. These results further strengthen the argument that model #20 is in best agreement. Table 3 summarizes the values of the constraints considered here for each solar model computed in this work. Listed are the Model, R_{env}, Y_{surf}, ^{8}B, $(Z/X)_{surf}$ and rms$(\delta c/c)$.

We conclude that of all the non-standard solar models listed in Tables 1 and 2, only models #15 and 16 are marginally acceptable. We can use these two models to set an upper limit to the amount of heavy element accretion during the early main sequence evolution of the Sun.

6. Discussion

There has been interest during the past few years in the effects of accretion on the Sun during its evolution. With this application in mind, the main purpose of this paper was to study the properties of a number of non-standard solar models in which the convection zone is richer in heavy elements than the interior, and to explore the constraints of helioseismology on such models.

A set of standard solar models were first constructed using the same physics and stellar evolution code as GD97, to serve as benchmarks for our non-standard models. Although our purpose was not to achieve the best possible fit to observation, we find that our standard solar model #20 satisfies the most stringent constraints from helioseismology at least as well as the best published standard solar model. It is just outside the 1σ limit for the $(Z/X)_{surf}$ constraint, but agrees very well with the SNO Collaboration ^{8}B neutrino flux. It is apparent that a standard solar model in full agreement with all up-to-date observational data would be achieved with the same physics as in GD97, for a Z_{init} intermediate between model #19 and model #20, i.e. for $0.020 < Z_{init} < 0.022$. It would also be interesting to probe intermediate values of Z_{int}, with $0.80 < Z_{int} < 1.00$.

For this work, we have only considered Z accretion from cometary material after the pre-MS phase, but what about the possibility of helium accretion as well, and increased accretion during an earlier, pre-MS era? If most of the accretion takes place in the pre-MS phase of solar evolution, we must consider two phases. In the early phase, the proto-Sun is fully or nearly fully convective (the Hayashi phase). Since the accreted material is mixed efficiently in the convective region, composition gradients in the deep interior would not be expected. In the later phase of pre-MS evolution (the Henyey phase), the radiative core gets progressively larger until the main sequence is reached. This phase of evolution, which takes place on a thermal timescale, is relatively short compared to diffusion timescales, and could leave behind a composition gradient in the interior, below the convection zone. Since we do not understand the region just below the present convection zone well, we cannot rule out the possibility of some composition in-homogeneity in the outer radiative envelope due to late pre-MS accretion. However, two factors argue against the existence of significant composition gradients in the outer envelope: (1) the presence of shear-induced turbulence in the tachocline region, and (2) the close agreement of the observed sound-speed and the SSM sound-speed in the radiative region below the tachocline layer.

None of our non-standard solar models agree as well with observation as our best standard models. But two of the least extreme non-standard solar models, models #15 and 16, come close to satisfying all of the observational constraints. For this reason, they provide a realistic upper limit of $\sim 2 M_\oplus$ of iron (or $\sim 40 M_\oplus$ of meteoric material) to the accretion experienced by the Sun during its early main sequence phase. This conclusion is compatible with Henney & Ulrich's (1998) earlier null result that the accretion of $8 M_\oplus$ of meteoric material on the Sun could not at this point be detected by seismology because of the uncertainties. Similarly, a solar enrichment of $0.5 M_\oplus$ in iron, as suggested recently by Murray et al. (2001), is beyond detectability by seismic means at the present time.

REFERENCES

Ahmad et al. 2001, Phys. Rev. Lett., 87, 071301

Asplund, M. 2000, A&A, 359, 755

Alexander, D. R., & Ferguson, J. W. 1994, ApJ, 437, 879

Bahcall, J. N. 1989, Neutrino Astrophysics (Cambridge: Cambridge Univ. Press)

Bahcall, J. N., & Pinsonneault, M. H. 1992, Rev. Mod. Phys., 60, 297

Bahcall, J. N., Pinsonneault, M. H., & Basu, S. 2001, ApJ, 555, 990

Basu, S. 1998, MNRAS, 298, 719

Basu, S. & Antia, H.M. 1997, MNRAS, 287, 189 (BA97)

Basu, S., Chaplin, W. J., Christensen-Dalsgaard, J., Elsworth, Y., Isaak, G. R., New, R., Schou, J., Thompson, M. J., & Tomczyk, S. 1997, MNRAS, 292, 243

Basu, S., Christensen-Dalsgaard, J. Schou, J., Thompson M. J., & Tomczyk, S. 1996, ApJ, 460, 1064

Basu, S., Pinsonneault, M.H., & Bahcall, J.N. 2000, ApJ, 529, 1084 (BPB00)

Bertello, L., Varadi, F., Ulrich, R. K., Henney, C. J., Kosovichev, A. G., García, R. A., & Turck-Chièze, S. 2000, ApJ, 537, 143

Chaboyer, B., Demarque, P., Guenther, D.B., & Pinsonneault, M.H. 1995, ApJ, 446, 435

Christensen-Dalsgaard, J., Gough, D.O., & Morgan, J.G. 1979, A&A, 73, 121

Christensen-Dalsgaard, J., Gough, D.O., & Thompson, M.J. 1991, ApJ, 378, 413

García, R. A., Bertello, L., Turck-Chièze, S., Couvidat, S., Gabriel, A.H., Henney, C. J., Régulo, C., Robillot, J. M., Roca Cortés, T., Ulrich, R. K., & Varadi, F. 2001, in Proc. SOHO 10/GONG 2000 Workshop: Helio- and Asteroseismology at the Dawn of the Millennium, ed A. Wilson (Noordwijk:ESA), 473

Grevesse, N., Noels, A. & Sauval, A.J. 1996, in ASP Conf. Ser.99, Cosmic Abundances, ed. S.S. Holt & G. Sonneborn (San Francisco:ASP), 117

Grevesse, N., & Sauval, A.J. 1998, Space Sci. Rev., 85, 161

Guenther, D.B. 1989, ApJ, 339, 1156

Guenther, D.B. 1994, ApJ, 422, 400

Guenther, D. B., Demarque, P., Kim, Y.-C., & Pinsonneault, M. H. 1992, ApJ, 387, 372

Guenther, D. B. & Demarque, P. 1997, ApJ, 484, 937 (GD97)

Henney, C.J., & Ulrich, R.K. 1998, in Structure and Dynamics of the Interior of the Sun and Sun-like Stars, ed. S. Korzennik & A. Wilson (Noordwijk:ESA), 473

Iglesias, C. A., & Rogers, F. J. 1996, ApJ, 464, 943

Jeffery, C. S., Bailey, M. E. & Chambers, J. E. 1997, The Observatory, 117, 224

Mathis, J. S. 1996, ApJ, 472, 643

Murray, N., Chaboyer, B., Arras, P., Hansen, B., & Noyes, R.W. 2001, ApJ, 555, 801

Rhodes, E.J. Jr., Kosovichev, A.G., Schou, J., Scherrer, P.H., & Reiter, J. 1997, Sol. Phys., 175, 287

Rogers, F. J. 1986, ApJ, 310, 723

Rogers, F. J., Swenson, F. J., & Iglesias, C. A. 1996, ApJ, 456, 902

Rood, R.T. 1978, in Proc. Informal Conf. Status and Future of Solar Neutrino Research, ed. G. Friedlander, BNL-50879, 1, 175

Turck-Chièze, S., Couvidat, S., Kosovichev, A. G., Gabriel, A. H., Berthomieu, G., Brun, A. S., Christensen-Dalsgaard, J., García, R. A., Gough, D. O., Provost, J., Roca-Cortés, T., Roxburgh, I. W., & Ulrich, R. K. 2001, ApJ, 555, 69

Table 1.   Solar Model Characteristics

Model	Type	X_{init}	Z_{init}	$Z_{\mathrm{int}}/Z_{\mathrm{init}}$	X_{surf}	Z_{surf}	M_{env}	R_{env}	$\log P_c$	$\log T_c$	$\log \rho_c$	X_c	Z_c
1	NSSM	0.8145	0.0170	0.30	0.8359	0.0153	0.02010	0.7139	17.354	7.160	2.148	0.468	0.0053
2	NSSM	0.8066	0.0188	0.30	0.8282	0.0170	0.02201	0.7071	17.356	7.162	2.151	0.460	0.0059
3	NSSM	0.8013	0.0200	0.30	0.8231	0.0181	0.02332	0.7026	17.357	7.163	2.153	0.456	0.0063
4	NSSM	0.7930	0.0220	0.30	0.8152	0.0199	0.02474	0.6982	17.358	7.165	2.155	0.448	0.0069
5	NSSM	0.7813	0.0170	0.50	0.8063	0.0153	0.02063	0.7164	17.361	7.170	2.160	0.431	0.0089
6	NSSM	0.7702	0.0188	0.50	0.7955	0.0169	0.02262	0.7102	17.364	7.173	2.165	0.420	0.0099
7	NSSM	0.7629	0.0200	0.50	0.7884	0.0180	0.02408	0.7057	17.366	7.175	2.168	0.413	0.0105
8	NSSM	0.7546	0.0220	0.50	0.7805	0.0198	0.02531	0.7020	17.367	7.178	2.170	0.405	0.0115
9	NSSM	0.7609	0.0170	0.65	0.7880	0.0153	0.02081	0.7185	17.366	7.177	2.168	0.408	0.0116
10	NSSM	0.7517	0.0188	0.65	0.7791	0.0169	0.02251	0.7130	17.367	7.180	2.171	0.399	0.0128
11	NSSM	0.7454	0.0200	0.65	0.7730	0.0180	0.02365	0.7094	17.368	7.181	2.173	0.393	0.0137
12	NSSM	0.7355	0.0220	0.65	0.7636	0.0198	0.02488	0.7061	17.370	7.184	2.176	0.384	0.0150
13	NSSM	0.7461	0.0170	0.80	0.7751	0.0153	0.02058	0.7211	17.368	7.182	2.172	0.392	0.0143
14	NSSM	0.7357	0.0188	0.80	0.7649	0.0169	0.02227	0.7157	17.370	7.185	2.176	0.382	0.0158
15	NSSM	0.7284	0.0200	0.80	0.7578	0.0180	0.02339	0.7124	17.371	7.187	2.178	0.374	0.0168
16	NSSM	0.7170	0.0220	0.80	0.7470	0.0198	0.02474	0.7088	17.373	7.191	2.182	0.363	0.0185
17	SSM	0.7265	0.0170	1.00	0.7577	0.0152	0.02041	0.7244	17.369	7.190	2.178	0.364	0.0179
18	SSM	0.7140	0.0188	1.00	0.7456	0.0169	0.02202	0.7199	17.371	7.194	2.182	0.349	0.0198
19	SSM	0.7057	0.0200	1.00	0.7376	0.0180	0.02325	0.7163	17.372	7.197	2.185	0.339	0.0210
20	SSM	0.6960	0.0220	1.00	0.7283	0.0198	0.02449	0.7128	17.373	7.201	2.188	0.327	0.0232

Table 2.   Solar Model Nuclear Data[a]

Model#	Fraction of Total Luminosity				Solar Neutrino Flux[b]									
	PPI	PPII	PPIII	CNO	PP $(\times 10^{10})$	PeP $(\times 10^8)$	HeP $(\times 10^3)$	^{7}Be $(\times 10^9)$	^{8}B $(\times 10^6)$	^{13}N $(\times 10^8)$	^{15}O $(\times 10^8)$	^{17}F $(\times 10^6)$	$\Phi(^{37}$Cl$)$	$\Phi(^{71}$Ga$)$
1	0.9490	0.0449	0.0038	0.0027	6.32	1.62	2.66	2.03	0.86	1.15	0.71	0.73	1.76	96.5
2	0.9461	0.0472	0.0040	0.0031	6.30	1.61	2.63	2.13	0.94	1.34	0.85	0.88	1.89	97.6
3	0.9441	0.0487	0.0041	0.0034	6.29	1.61	2.61	2.20	1.00	1.47	0.95	0.99	1.98	98.3
4	0.9408	0.0512	0.0043	0.0040	6.28	1.60	2.57	2.32	1.10	1.70	1.13	1.18	2.13	99.6
5	0.9343	0.0585	0.0049	0.0027	6.25	1.57	2.50	2.65	1.44	1.09	0.77	0.82	2.54	102
6	0.9288	0.0630	0.0053	0.0033	6.23	1.56	2.45	2.85	1.67	1.31	0.96	1.03	2.85	104
7	0.9250	0.0661	0.0056	0.0037	6.21	1.55	2.42	2.99	1.83	1.48	1.11	1.20	3.08	105
8	0.9204	0.0697	0.0059	0.0044	6.19	1.53	2.38	3.16	2.04	1.75	1.33	1.45	3.36	107
9	0.9233	0.0690	0.0058	0.0024	6.21	1.53	2.39	3.12	2.00	0.93	0.71	0.77	3.25	106
10	0.9180	0.0733	0.0062	0.0029	6.19	1.52	2.35	3.32	2.27	1.12	0.87	0.96	3.60	108
11	0.9143	0.0764	0.0064	0.0032	6.17	1.51	2.32	3.46	2.48	1.26	1.00	1.10	3.87	109
12	0.9080	0.0815	0.0069	0.0040	6.14	1.49	2.28	3.70	2.83	1.52	1.23	1.37	4.33	112
13	0.9142	0.0779	0.0066	0.0016	6.17	1.50	2.31	3.53	2.58	0.63	0.50	0.55	3.96	109
14	0.9076	0.0837	0.0070	0.0020	6.14	1.48	2.27	3.79	2.99	0.78	0.63	0.71	4.48	112
15	0.9027	0.0879	0.0074	0.0023	6.12	1.47	2.23	3.99	3.32	0.88	0.73	0.82	4.89	114
16	0.8946	0.0949	0.0080	0.0029	6.09	1.45	2.18	4.31	3.90	1.09	0.92	1.05	5.61	118
17	0.8911	0.0911	0.0077	0.0106	6.06	1.45	2.19	4.13	3.60	3.99	3.35	3.78	5.46	120
18	0.8793	0.0992	0.0084	0.0136	6.00	1.42	2.13	4.50	4.33	5.07	4.35	4.97	6.42	126
19	0.8708	0.1048	0.0088	0.0160	5.96	1.40	2.08	4.76	4.88	5.92	5.16	5.93	7.15	130
20	0.8595	0.1116	0.0094	0.0199	5.90	1.38	2.03	5.07	5.63	7.30	6.48	7.50	8.16	136

[a]1-16 Non-Standard Solar Models, 17-20 Standard Solar Models

[b]Values given in units of cm^{-2}s^{-1}, except $\Phi(^{37}$Cl$)$ and $\Phi(^{71}$Ga$)$, which are given in SNU.

Table 3.   Solar Model Constraint Values[a]

Model	R_{env}	Y_{surf}	^8B	$(Z/X)_{surf}$	$rms(\delta c/c)$
1	0.7139	0.1488	0.86	0.0183	0.0123
2	0.7071	0.1548	0.94	0.0205	0.0114
3	0.7026	0.1588	1.00	0.0220	0.0111
4	0.6982	0.1649	1.10	0.0244	0.0106
5	0.7164	0.1784	1.44	0.0190	0.0084
6	0.7102	0.1876	1.67	0.0212	0.0070
7	0.7057	0.1936	1.83	0.0228	0.0063
8	0.7020	0.1997	2.04	0.0254	0.0060
9	0.7185	0.1967	2.00	0.0194	0.0064
10	0.7130	0.2040	2.27	0.0217	0.0052
11	0.7094	0.2090	2.48	0.0233	0.0046
12	0.7061	0.2166	2.83	0.0259	0.0041
13	0.7211	0.2096	2.58	0.0197	0.0056
14	0.7157	0.2182	2.99	0.0221	0.0040
15	0.7124	0.2242	3.32	0.0238	0.0031
16	0.7088	0.2332	3.90	0.0265	0.0022
17	0.7244	0.2271	3.60	0.0201	0.0050
18	0.7199	0.2375	4.33	0.0227	0.0029
19	0.7163	0.2444	4.88	0.0244	0.0015
20	0.7128	0.2519	5.63	0.0272	0.0006

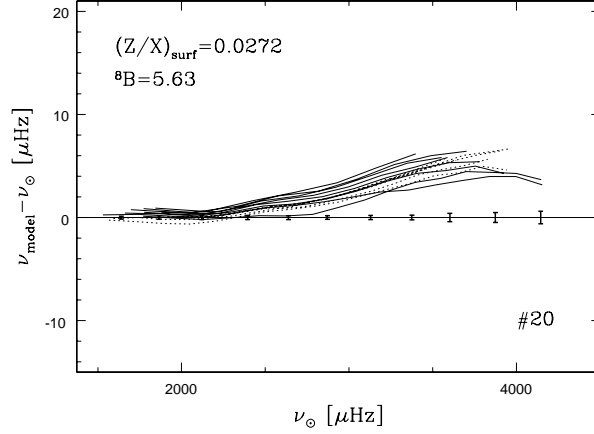[a]1-16 Non-Standard Solar Models, 17-20 Standard Solar Models
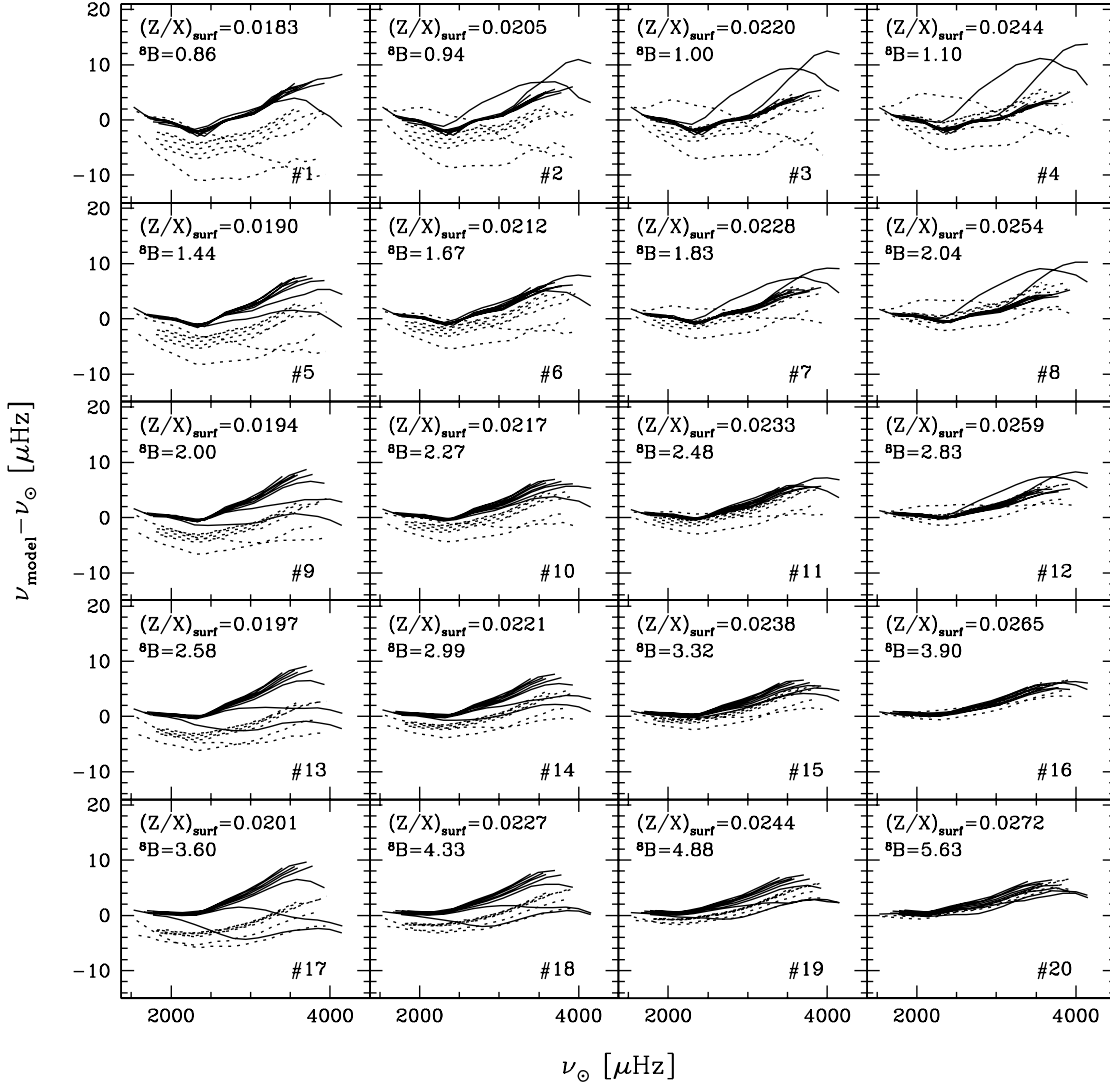
Fig. 1.— Grid of *p*-mode frequency difference plots, (model - Sun), for all models computed in this work. Lines connect data with a common *l*-value. Dashed lines correspond to *l*=0-4, 10 and 20. Solid lines correspond to *l*=30, 40, 50, 60, 70, 80, 90, and 100. Each plot is annotated with the corresponding model number (see Tables 1-3), the surface Z/X ratio, and the ^{8}B neutrino flux, in cm^{-2}s^{-1}. Observational data used are from the MDI-SOHO data set (Rhodes et al. 1997).

Fig. 2.— p-mode frequency difference plot, (model - Sun), for model #20 computed in this work. Lines connect data with a common l-value. Dashed lines correspond to l=0-4, 10 and 20. Solid lines correspond to l=30, 40, 50, 60, 70, 80, 90, and 100. Listed are the surface Z/X ratio and the ^{8}B neutrino flux, in $cm^{-2}s^{-1}$. Observational data used are from the MDI-SOHO data set (Rhodes et al. 1997). The error bars indicate 10σ errors in the data, averaged over 250μHz frequency bins, for all l-values included in this work.
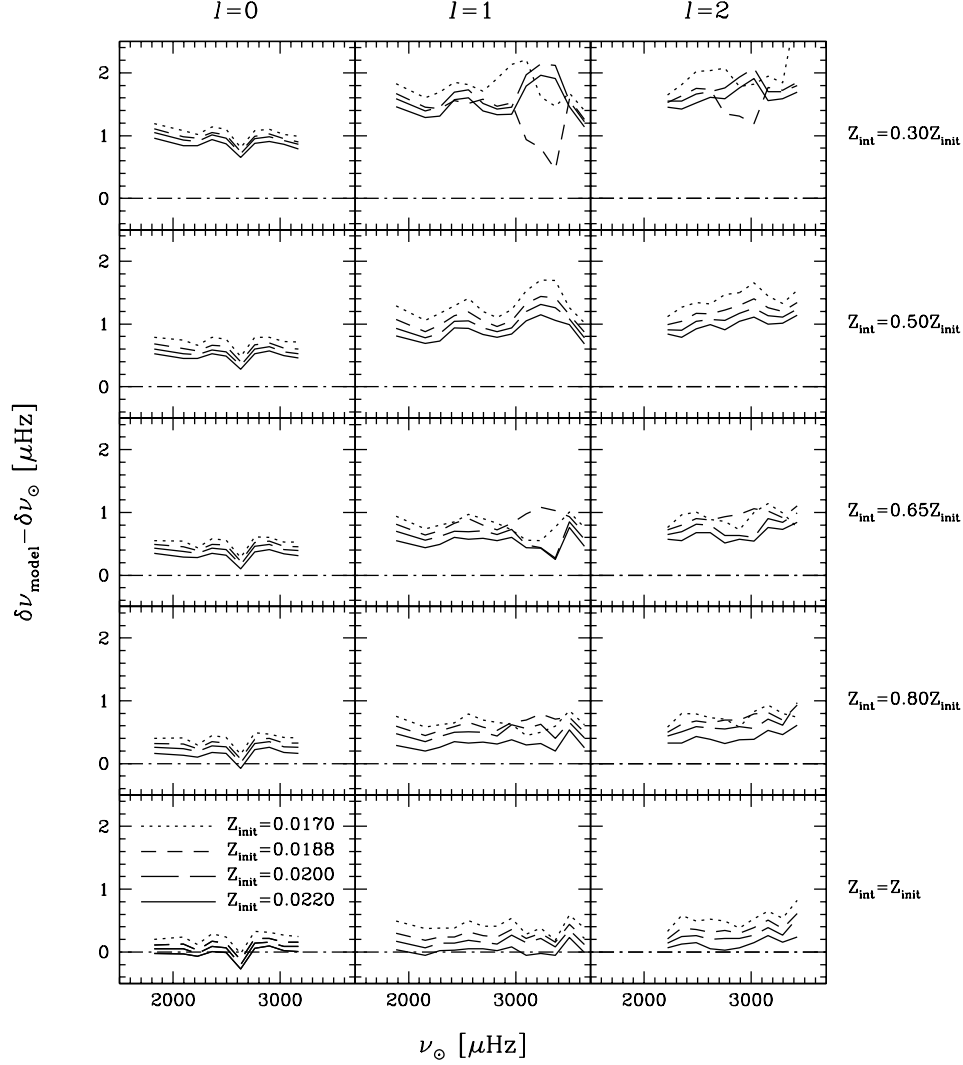
Fig. 3.— Grid of small spacing difference plots, (model - Sun), for all models computed in this work. Lines connect data from a particular model, indicated by Z_{int} and Z_{init}. Each row contains models of the same Z_{int}, where $Z_{int}=0.30Z_{init}$ includes models #1-4, $Z_{int}=0.50Z_{init}$ includes models #5-8, $Z_{int}=0.65Z_{init}$ includes models #9-12, $Z_{int}=0.80Z_{init}$ includes models #13-16, and $Z_{int}=Z_{init}$ includes the standard solar models #17-20. Each column contains results for a common l-value, with $l=0$ in column 1, $l=1$ in column 2, and $l=2$ in column 3. Observational data used are from the MDI-SOHO data set (Rhodes et al. 1997).
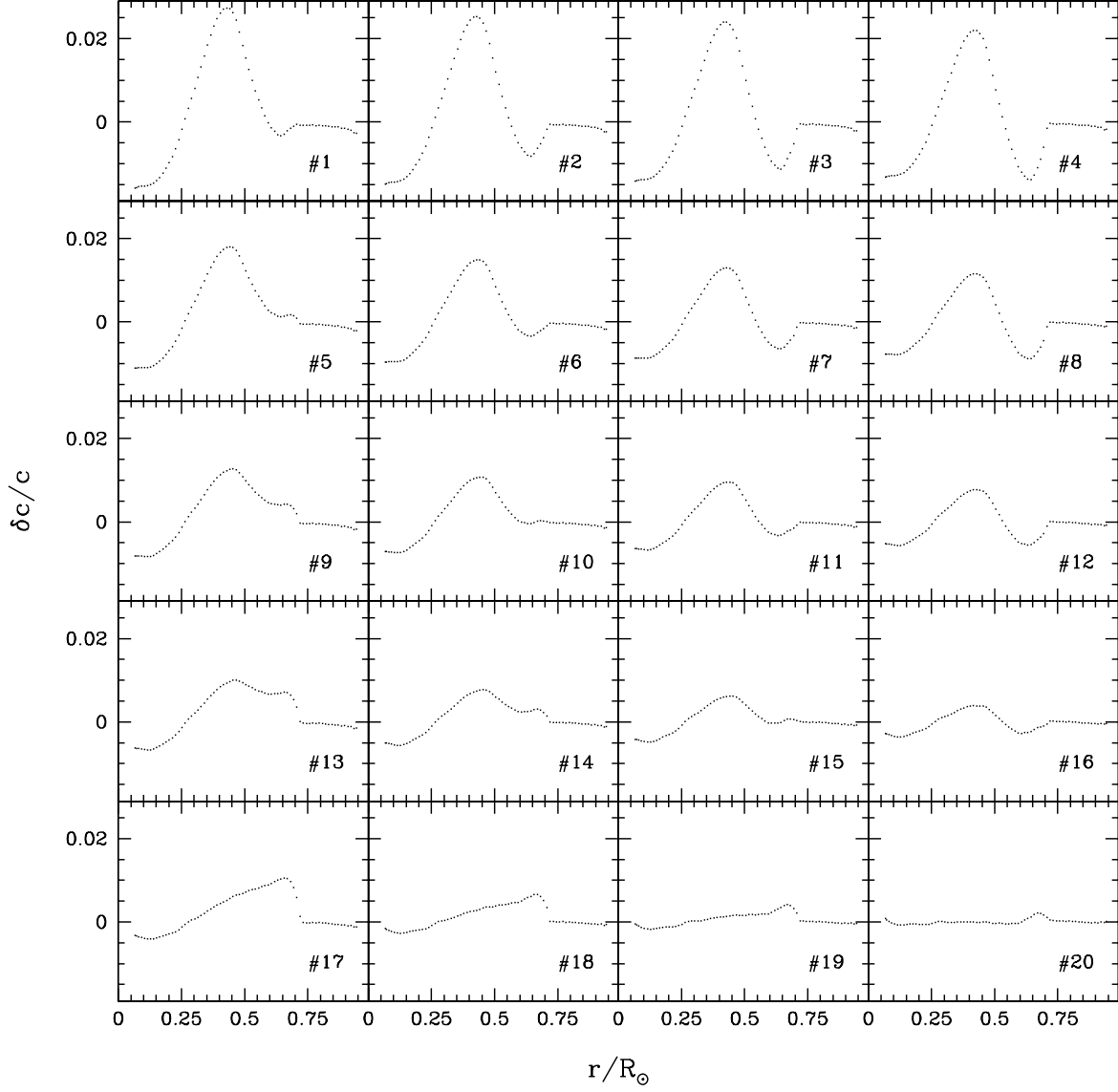
Fig. 4.— Grid of fractional difference plots for the sound-speed ((Sun - model)/model), for all models computed in this work. Solar sound-speed data were determined by Basu, Pinsonneault & Bahcall (2000) using the MDI-SOHO solar frequency data set (Rhodes et al. 1997).
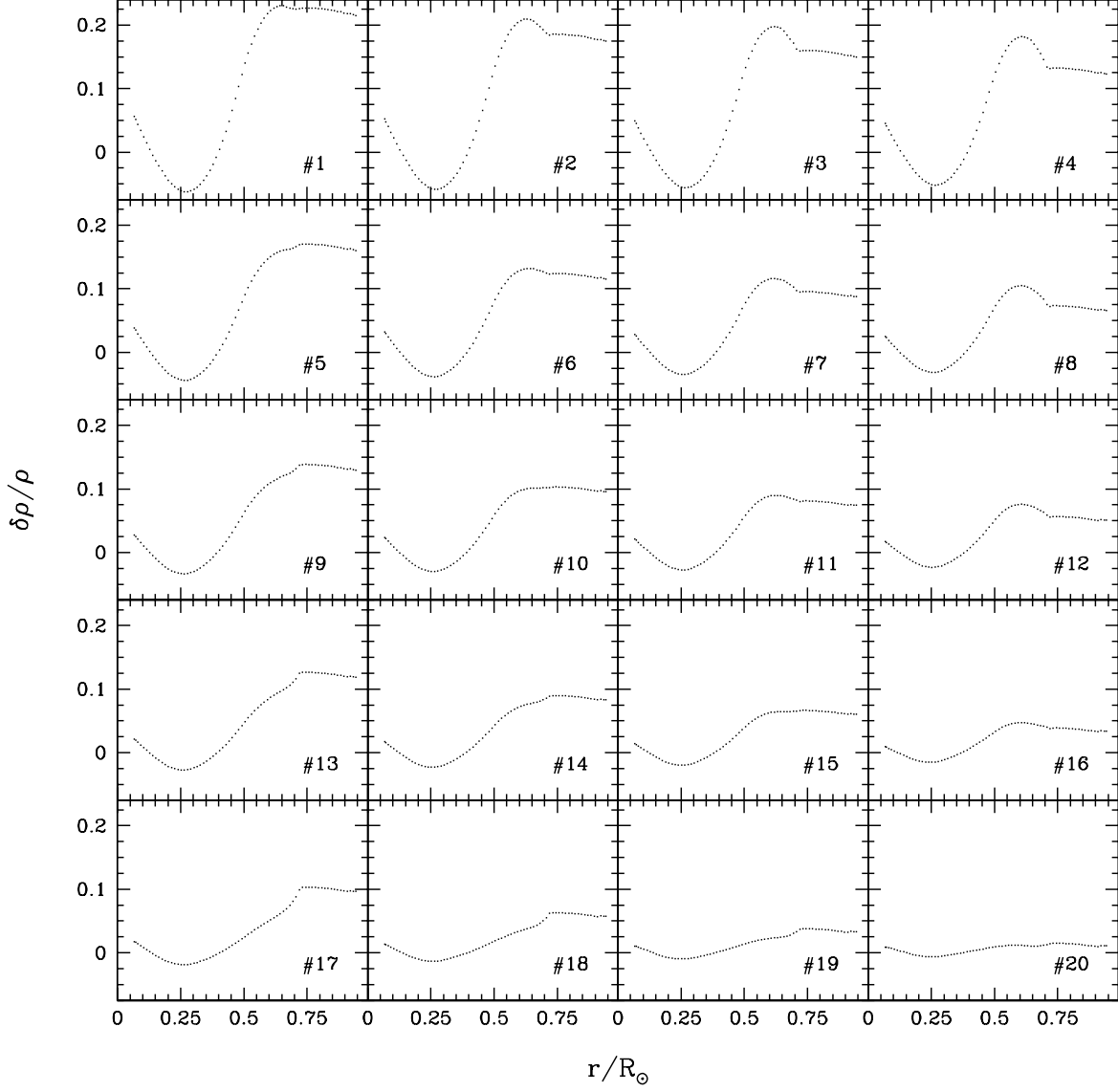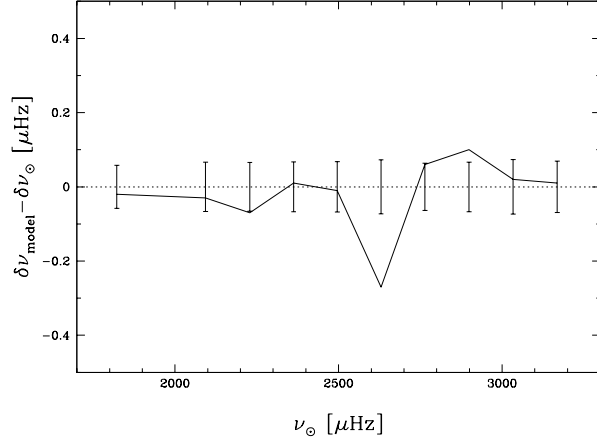
Fig. 5.— Grid of fractional difference plots for density ((Sun - model)/model), for all models computed in this work. Solar density data were determined by Basu, Pinsonneault & Bahcall (2000) using the MDI-SOHO solar frequency data set (Rhodes et al. 1997).

Fig. 6.— Small spacing difference plot (model - Sun), for standard solar model #20 with l=0. Observational data used are from the MDI-SOHO data set (Rhodes et al. 1997). The error bars plotted represent errors in the data. The observational uncertainties are approximately ± 0.07 μHz for the small spacing determination.
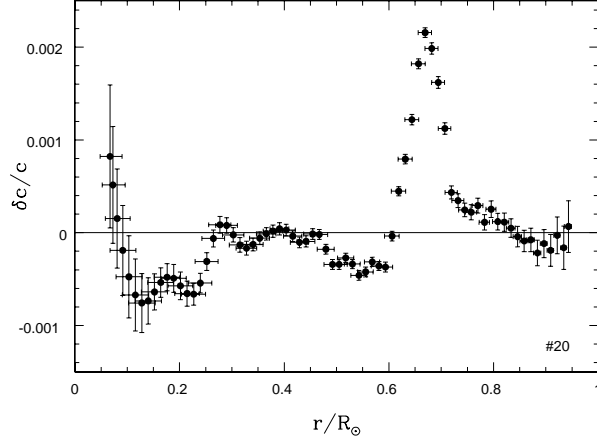
Fig. 7.— Fractional difference plot for the sound-speed ((Sun - model)/model), for standard solar model #20 (zoom in of Figure 4). Vertical error bars indicate 1σ errors in the inversion results due to errors in the data. Horizontal error bars are a measure of the resolution of the inversion.
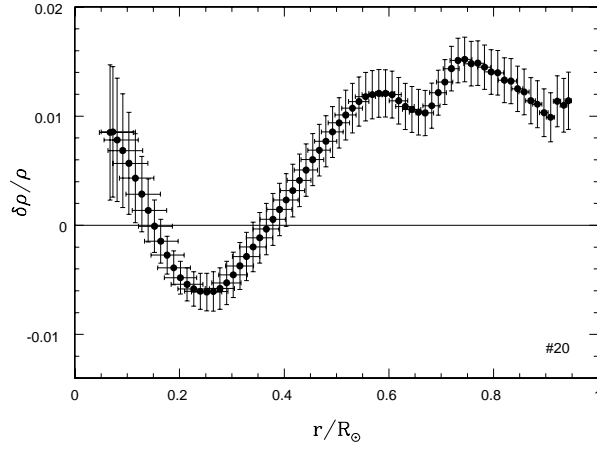

Fig. 8.— Fractional difference plot for density ((Sun - model)/model), for standard solar model #20 (zoom in of Figure 5).